Materials Advances

ROYAL SOCIETY OF CHEMISTRY

PAPER

View Article Online
View Journal | View Issue

Cite this: *Mater. Adv.*, 2023, 4, 5653

A multivariate metal–organic framework based pH-responsive dual-drug delivery system for chemotherapy and chemodynamic therapy†

Muhammad Usman Akbar,[ab] Arslan Akbar,[b] Umair Ali Khan Saddozai,[c] Malik Ihsan Ullah Khan,[d] Muhammad Zaheer*[b] and Muhammad Badar*[a]

Received 10th July 2023,
Accepted 8th October 2023

DOI: 10.1039/d3ma00389b

rsc.li/materials-advances

Combination therapy has emerged as a promising strategy due to its synergistic therapeutic pathways that enhance anticancer efficacy and limit the emergence of drug resistance. In this work, MIL-88B type multivariate (MTV-1) nanocarriers based on a mixed linker (1,4-benzenedicarboxylic acid and biphenyl-4,4′-dicarboxylic acid) and metals (iron and cobalt) were synthesized. The presence of the distinct linkers modified the pore makeup of MTV-1 and facilitated the co-encapsulation of two anticancer drugs of varying molecular sizes: 5-fluorouracil (5-FU) and curcumin (CUR). The drug loading measurements on MTV-1@5-FU + CUR represented a loading capacity of 15.9 wt% for 5-FU and 9.3 wt% for CUR, respectively. They further exhibited a pH-responsive drug release pattern with higher concentrations of 5-FU and CUR released at pH 5.5 (simulating cancer microenvironment) compared to pH 7.4 (physiological environment). Moreover, we also demonstrated that MTV-1 MOFs, due to the presence of mixed valence metal ions, could exhibit peroxidase-like activity and catalyze H_2O_2 decomposition to produce $^{\bullet}OH$ radicals for chemodynamic therapy. Cell cytotoxicity assays exhibited significant inhibitory effects of MTV-1@5-Fu + CUR against HepG2 cells with an IC_{50} of 78.7 μg mL^{-1}. With dual-drug loading, pH-responsive release, and chemodynamic therapy, MTV-1 shows excellent potential for multifunctional anticancer treatment.

Introduction

Cancer has remained one of the leading causes of death worldwide.[1] The main hurdles to overcoming this issue lie in the widely used traditional chemotherapies based on monotherapeutics.[2] The poor delivery mechanisms and insufficient distribution of drugs in an intracellular environment have aggravated the problem.[3] The emergence of drug resistance, target site mutagenesis, and interconnected resistance pathways further mitigates the efficacy of drugs designed to act on singular molecular pathways.[4] Recently, using multiple drugs against a single target, also known as combination therapy, has shown promising results in alleviating these problems.[5–8] Combination therapy offers multiple therapeutics in a single treatment and benefits from their distinct modes of action for enhanced anticancer activity.[9] Various drug delivery carriers, such as liposomes,[10] supramolecular nanoparticles,[11] polymers,[12] layered double hydroxides (LDHs),[13] and mesoporous silica,[14] have been employed for multi-drug delivery. Among all the present nanocarriers, metal–organic frameworks (MOFs), have attracted much attention for drug delivery applications.[15–20] MOFs are constructed through the coordination between metal ions and organic linkers, also known as secondary building units (SBUs).[21] When used as drug delivery systems (DDSs), MOFs can prolong the drug release period,[22] enhance drug solubility,[23] improve the antitumor effect,[24] and bring a pharmacokinetic change in the drug delivery pattern.[25,26]

Moreover, synthetic or post-synthetic modifications can turn the MOFs into stimuli-responsive nanocarriers to release their payload against external (temperature, irradiation, and pressure) or internal (redox reaction, pH, ATP, and H_2S) stimuli.[27–31] Additionally, chemical constituents of MOFs can be manipulated to utilize higher levels of reactive oxygen species (ROS) produced in cancer cells for chemodynamic therapy.[32–35] Compared to

[a] *Gomal Center of Biochemistry and Biotechnology, Gomal University, Dera Ismail Khan, 29050, Pakistan. E-mail: mbadar@gu.edu.pk*
[b] *Department of Chemistry and Chemical Engineering, Syed Babar Ali School of Science and Engineering, Lahore University of Management Sciences (LUMS), Lahore, 54792, Pakistan. E-mail: muhammad.zaheer@lums.edu.pk*
[c] *Department of Preventive Medicine, Institute of Biomedical Informatics, Bioinformatics Center, Henan Provincial Engineering Center for Tumor Molecular Medicine, School of Basic Medical Sciences, Henan University, Kaifeng 475004, China*
[d] *Institute of Molecular Biology and Biotechnology, The University of Lahore, Lahore, 54000, Pakistan*

† Electronic supplementary information (ESI) available. See DOI: https://doi.org/10.1039/d3ma00389b

normal cells, cancer cells generate more ROS (especially H_2O_2) stress due to mitochondrial malfunction and metabolic activity.[36–38] ROS is usually classified into singlet oxygen ($^1O_2$), hydroxyl radicals ($^{\bullet}OH$), hydrogen peroxide (H_2O_2) and superoxide anion radical ($O_2^{\bullet-}$).[39,40] Moreover, with coordination complexes containing divalent or trivalent metal ions such as Iron (Fe), Cobalt (Co), Manganese (Mn), Cerium (Ce) and Copper (Cu), H_2O_2 can be decomposed into highly potent $^{\bullet}OH$ radicals through Fenton and Fenton-like reactions.[41,42] These $^{\bullet}OH$ radicals are highly reactive and can cause lipid peroxidation, DNA damage and oxidation of proteins.[43–45] Compared to monometallic molecules, the presence of two or more different metals in coordination compounds, in many cases, has demonstrated enhanced catalytic performance due to the synergistic effect between the metals.[46,47] For instance, the presence of a Fe–Cu complex (heme proteins) and Mo–Fe proteins in the human body plays an essential role in cytochrome and nitrogenase oxidation metabolic pathways.[48,49] The coexistence of different metals and their synergism in some cases becomes indispensable for efficient catalytic properties of the enzymes.[50] Similar to naturally found bimetallic enzymes, mixed metal MOFs have also demonstrated improved catalytic performance due to the synergistic effect between different metals.[51,52] The Fenton-like performance of Fe-based MOFs largely depends upon the concentration of divalent Fe^{2+} in the system and cycling between Fe^{2+} and Fe^{3+} and *vice versa*.[53] However, achieving an appropriate ratio of Fe^{2+} and Fe^{3+} metals in MOF synthesis is troublesome and leads to the formation of an amorphous product or requires thermal reduction resulting in defective MOFs.[54] Therefore, synthesizing mixed metal MOFs with controlled architecture using pre-synthesized mixed metal clusters containing trivalent Fe^{3+} and divalent second metal (M^{II}) is considered a viable option. The pre-synthesized mixed-metal cluster exhibits a highly defined stoichiometric ratio of both metals, plus the excellent electron transfer between different metals further improves the catalytic performance of the designed framework.[55]

Although MOFs have made some progress in chemodynamic therapy,[56] their use for combination therapy is limited.[57] One of the main reasons behind the low utility of MOFs for combination therapy is the use of analogous SBUs (organic/inorganic) in MOF synthesis, leaving less room for pore engineering and modifications.[58,59] To overcome this, multi-component/multivariate (MTV) MOFs have recently emerged as an alternative solution to the problem.[60,61] In MTV MOFs, more than one type of SBU (linker and metal) are intertwined chemically in a singular framework; maintaining the structural traits of the parent MOF while altering the physico-chemical environment.[62,63] Using multiple SBUs helps tailor the pore environment to co-encapsulate different drugs and release them through engineered chemical functionalities.[64,65] Minor alterations in the SBUs can bring macroscopic changes and result in a variety of MTV-MOFs synthesized with targeted properties.[66] Due to these characteristics, MTV-MOFs have been proving their mettle in the fields of gas storage,[67] luminescence sensing,[68] and heterogeneous catalysis.[69] However, their potential for multi-drug delivery and chemodynamic therapy hasn't been fully explored.

5-Fluorouracil (5-FU) is a hydrophilic (pyrimidine analog) anticancer drug used to treat a variety of tumors through DNA/RNA disruption.[70] However, 5-FU is non-specific to targets, and its rapid degradation rate (5–10 min) leads to the inadequate presence of the drug in cancer cells,[71] which has reduced its efficacy and led to the emergence of multi-drug resistance (MDR).[72] To overcome this issue, 5-FU has been combined with other drugs, such as paclitaxel, cisplatin, and curcumin (CUR), to improve cytotoxicity and reduce dosage requirements.[73–75] CUR, a natural polyphenol chemotherapeutic agent, has shown great potential for antioxidant, antimicrobial, and antitumor purposes.[76–79] CUR induces anticancer effects by initiating various signalling (*e.g.*, PI3K/Akt, STAT3, and NF-kB) pathways inducing apoptosis.[80,81] However, free CUR cannot be administered directly due to its poor bioavailability and high hydrophobicity, requiring carriers for the delivery to the target site.[82]

To co-encapsulate 5-FU and CUR by pore engineering, we synthesized MTV-1 MOFs with variable pore sizes by introducing a sizeable ratio of biphenyl 4-4, dicarboxylic acid (BPDC) into mono linker FeCo-MIL-88B MOFs through an isoreticular expansion strategy. Fe and Co-based mixed-metal clusters were used in the synthesis process due to their accessible Lewis acid sites for drug adsorption and peroxidase-like activity of both metals. The drug loading capacity (DLC) and drug loading efficiency (DLE) of MTV-1@5-FU + CUR were measured to be 15.9 and 18.1 wt% for 5-FU and 9.3 and 10.5 wt% for CUR. Mathematical kinetic release models were applied to fit the nanocarriers' drug release pattern at different pHs (pH = 7.4 for normal tissues and pH = 5.5 for the tumor cell environment). Moreover, the *in vitro* cytotoxicity profile of MTV-1 based on chemotherapy and chemodynamic therapy was evaluated against HEK-293 and HepG2 cell lines.

Materials and methods

Materials

Iron(III) nitrate nonahydrate ($Fe(NO_3)_3{\cdot}9H_2O$), cobalt(II) nitrate hexahydrate ($Co(NO_3)_3{\cdot}6H_2O$), 1,4-benzenedicarboxylic acid (BDC), biphenyl-4,4′-dicarboxylic acid (BPDC), sodium acetate trihydrate ($CH_3COONa\cdots3H_2O$), 5-fluorouracil (5-FU), curcumin (CUR), 3,3′,5,5′-tetramethylbenzidine (TMB) and *N*,*N*-dimethylformamide (DMF), glutaraldehyde, crystal violet, glacial acetic acid, Tween-80 and phosphate buffer saline (PBS) tablets were purchased from Sigma-Aldrich. Dulbecco's modified Eagle's medium (DMEM), fetal bovine serum (FBS), penicillin–streptomycin (pen-strep), trypsin-EDTA, L-glutamine and 3-(4,5-dimethylthiazol-2-yl)-2,5-diphenyltetrazolium bromide (MTT) were obtained from Gibco, Invitrogen. All of the chemicals were used as received.

Characterization

The morphology of the samples was characterized using a scanning electron microscope (SEM) FEI NOVA Nano SEM 450 equipped with energy dispersive X-ray spectroscopy (EDX). Samples were coated with gold prior to imaging. The metal composition and leaching analysis was performed through

inductively coupled plasma-optical emission spectroscopy (ICP-OES) using an Agilent Technologies 5110-svdv ICP-OES system. Zeta potential (ZP) was determined in water medium at room temperature using Malvern zetasizer (Nano ZS, Malvern). The crystal structure was analysed through an X-ray diffraction (XRD) pattern over a 2θ range from 5–50° obtained on BRUKER D2 Phaser using Ni-filtered Cu-Kα irradiation (λ = 1.5406 Å). The Brunauer–Emmett–Teller (BET) method was used to calculate the surface area at 77 K using a Quantachrome Nova 2200e. Bruker Alpha Platinum ATR was used to perform infrared spectroscopic studies in the 400–4000 cm^{-1} range. The thermal behaviour of the samples was assessed through Thermogravimetric analysis (TGA) using a TA instrument in the range of 10 to 600 °C (10° min^{-1} ramp) under an N_2 atmosphere. UV-Vis spectroscopic studies were performed to verify drug loading, release, and TMB oxidation using a spectrophotometer (Shimadzu UV-1800). The fluorometric measurements in the TA probe were carried out on a PerkinElmer Enspire 2300 multimode reader at an emission wavelength of 435 nm (λ_{ex} 315 nm). Cellular uptake and intracellular ROS-based studies through fluorescence imaging were performed using a confocal laser scanning microscope (CLSM) LSM-880 ZEISS, Jena, Germany.

Synthesis of FeCo-clusters

Bi-metallic (FeCo) clusters were synthesized using a previously reported method with slight modifications.[83] A solution of $CH_3COONa{\cdot}3H_2O$ (6 g, 0.044 mol) in 10 mL of deionized water was prepared (solution-1). Additionally, $Fe(NO_3)_3{\cdot}9H_2O$ (1.142 g, 0.0028 mol) and $Co(NO_3)_2{\cdot}6H_2O$ (4.154 g, 0.014 mol) were mixed separately in 10 mL of deionized water (solution-2). Later, solution-1 was added dropwise into a filtered and stirred solution-2. The mixture was allowed to react for 24 h with mild stirring at room temperature. After 24 h, the brown precipitates were filtered and washed with a small amount of ethanol. Later, the filtrate was allowed to air dry at room temperature.

Synthesis of nanocarriers

To synthesize the FeCo-MIL-88B MOF, equal masses of the FeCo-cluster (200 mg) and BDC (200 mg) were dissolved separately in 11 mL of DMF each. Samples were sonicated until the cluster and linker were dissolved. Later, the linker solution was added dropwise into the stirred solution of the cluster containing an additional 1 mL of glacial acetic acid. The mixture solution was kept under mild stirring until a homogenous solution was obtained that was transferred to an autoclave with a 50 mL capacity and incubated for 24 h at 120 °C. After 24 h, precipitates were collected through centrifugation and washed thrice with DMF and ethanol. The same methodology synthesized four additional MOFs except for the addition of different concentrations of BPDC in the linker mixture. The BPDC to BDC percentage in additional experiments was kept at 25, 50, 75, and 100%, and the synthesized MOFs were subsequently called MTV-1, MTV-2, MTV-3, and FeCo-MIL-88D.

Drug loading and release

All nanocarriers were activated under vacuum at 100 °C for 24 h before drug loading experiments. Initially, three different types of synthesized MOFs were selected for drug-loading experiments, namely FeCo-MIL-88B, MTV-1, and FeCo-MIL-88D. Briefly, 60 mg of activated MOFs were dispersed in 30 mL of 5-FU (2 mg mL^{-1}) and CUR (2 mg mL^{-1}) solution and left for 48 h under mild stirring. After 48 h, drug-loaded MOFs were isolated through centrifugation. The absorbance of the supernatant was determined using a UV-Vis spectrophotometer with the corresponding characteristic peaks of 5-FU (265 nm) and CUR (435 nm). The calibration curve of 5-FU and CUR in ethanol was applied to determine the drug loading capacity (DLC) and drug loading efficiency (DLE) according to the following equations:[84]

$$\mathrm{DLC\ (wt\%)} = \frac{\text{Weight of the loaded drug}}{\text{Total weight of drug} - \text{loaded MOFs}} \times 100 \quad (1)$$

$$\mathrm{DLE\ (wt\%)} = \frac{\text{Weight of the loaded drug}}{\text{Total weight of the feeding drug}} \times 100 \quad (2)$$

Based on the drug loading experiments (Table S2, ESI†) only MTV-1 MOFs loaded with 5-FU and CUR were further used for drug release studies. Drug release experiments were conducted under different pH conditions (5.5 and 7.4) in PBS with 1% (v/v) Tween 80. Briefly, a concentrated solution of MTV-1@5-FU + CUR (15 mg) was inserted into a dialysis bag (3.5 kDa MWCO) and dialyzed against 30 mL of PBS + 1% (v/v) Tween 80 solutions of pH 5.5 and 7.4. At predetermined time intervals, 1 mL of the solution containing the released drug was withdrawn and replaced with an equal amount of preheated PBS + 1% (v/v) Tween 80 solution to keep the volume constant. The isolated solutions were analyzed using UV-Vis spectroscopy to measure the amount of 5-FU and CUR according to the calibration curve of each drug drawn in the same buffer. The experiments were performed in duplicate, and the results are presented as an average. The cumulative drug release percentage was expressed as

$$C_c = C_t + \frac{v}{V}\sum_{0}^{t-1} C_t \quad (3)$$

$$\text{Drug release } (\%) = \frac{M_R}{M_L} \times 100\% \quad (4)$$

In eqn (3), C_c represents an adjusted concentration of CUR at time t, C_t represents the measured concentration of 5-FU/CUR at time t, v is the volume of the withdrawn sample, and V is the volume of the release solution. In eqn (4), M_R represents the released drug, and M_L represents the loaded drug concentrations.

Cell culture

Human embryonic kidney cells (HEK-293 cells) and Human Hepatoma cells (HepG2 cells) were supplied by The University of Lahore (UOL) Cell Culture Collection (UCCC). The cells were cultured in DMEM supplemented with 10% Hi-FBS, 1% Pen-strep (100 IU mL^{-1} penicillin and 100 μg mL^{-1} streptomycin), 2 mM L-glutamine, and 1% non-essential amino acids.

Cells were grown in cell culture flasks in a humidified atmosphere at 37 °C supplemented with 5% CO_2. Cells were sub-cultured in a 1 : 3 split ratio with 0.25% trypsin-EDTA (1–2 mL) treatment every 3–5 days.

Cell viability test

The *in vitro* cytotoxicity of the samples against HEK-293 and HepG2 cell lines was evaluated through MTT assay.[85] Briefly, HepG2 and HEK-293 cells (100 μL) with a density of 1×10^4 were seeded (triplicates) in a 96-well plate. The cells were incubated for 24 h at 37 °C in a CO_2 incubator. After that, the cell culture medium was removed, and different concentrations (3.9 to 500 μg mL^{-1}) of 5-FU, CUR, MTV-1, and MTV-1@5-FU + CUR dissolved in the culture medium were added to the cells. In comparison, the cells in the control groups were not treated with any of the compounds. After 48 h of incubation, 10 μL of MTT (12 mM) reagent was added to each well, and the cells were allowed to incubate for another 4 h. After that, the medium was removed, and formazan was dissolved by adding 100 μL of DMSO. The absorbance was recorded at 570 nm using a PerkinElmer Enspire 2300 multimode reader (Germany). The treatment groups' IC_{50} (half maximal inhibitory concentration) values were calculated through non-linear regression using a dose–response curve. To evaluate cell viability in the presence of H_2O_2 for peroxidase-like activity, the cells were co-cultured with different concentrations of MTV-1, H_2O_2 (200 μM), and MTV-1 + H_2O_2 (200 μM) according to the same procedure.

Colony formation assay

The long-term cytotoxic profile of the synthesized system was evaluated through a colony formation assay. Briefly, HepG2 cells with a density of 1000 cells per well were seeded into 6-well plates in 2 mL of medium containing 10% FBS. The cells were allowed to initiate colonies for two days. Later, these cells were treated with the desired concentrations of 5-FU, CUR, MTV-1, and MTV-1@5-FU + CUR for eight days under a humidified atmosphere at 37 °C in 5% CO_2. The cells were rinsed with PBS. A mixture of 0.5% crystal violet and 6% glutaraldehyde was added, and cells were left for 30 min. Later, the added mixture was removed carefully and plates containing colonies were left to dry at room temperature. After that, photographs were taken and colonies were counted.

Cellular uptake studies

Due to the intrinsic green fluorescence of CUR, CLSM imaging was used to investigate the cellular uptake of MTV-1@5-FU + CUR. For this, the HepG2 cells with a density of 1×10^4 were grown in 24 well plates for 24 h. After that, the previous medium was replaced with fresh medium containing MTV-1@5-FU + CUR solution (40 μg mL^{-1}). The cells were allowed to incubate for 48 h. Then, the culture medium was sucked out, and cells were washed with PBS twice and fixed with 4% formalin. Later, cells were stained with DAPI solution for 25 min in the dark at 37 °C and visualized under CLSM.

Peroxidase-like activity assay

The peroxidase-like activity was determined by the amount of TMB oxidation that occurred in the process.[86] Briefly, 5 ml of weak acidic PBS (pH 5.5) was prepared containing different amounts of MTV-1 MOFs (0, 20, 40, 60, 80, and 100 μg mL^{-1}), TMB (0.25 mM), and H_2O_2 (1 mM). The mixture was incubated for 10 min at 37 °C. After that, UV-vis spectroscopic spectra of the samples at a 652 nm wavelength corresponding to the oxidized TMB in the solution were obtained. Furthermore, the peroxidase-like activity of the MTV-1 MOFs was further checked by varying the pH (4–8) and temperature (30–60 °C) of the solution, keeping the concentration of the MOFs (60 μg mL^{-1}) constant.

Intracellular ROS generation

HepG2 cells with a density of 3×10^4 cells were seeded into a 12-well confocal dish and incubated for 24 h at 37 °C (5% CO2) for intracellular ROS detection. After 24, the previous medium was replaced with fresh and different treatments of PBS, MTV-1 (50 μg mL^{-1}) + H_2O_2 (100 μM) at pH 7.4 and 6.5 were applied to the cells for 4 h. Then, cells were washed with fresh medium, followed by the addition of DCFH-DA solution (25 μM), and incubated for another 1 h under dark conditions. Later, the cells were washed with PBS, and nuclei were stained with DAPI. The intracellular $^{\bullet}OH$ generation was examined under a CLSM by measuring the fluorescence of DCFH (λ_{ex} = 488 nm, λ_{em} = 525 nm).

Metal leaching experiment

MTV-1 (0.50 mg mL^{-1}) was immersed in phosphate buffers (pH 7.4 and 5.5) at 37 °C for 1, 2, 4, 6, 12 and 24 h.[87] After each predetermined interval of time, samples were centrifuged for 20 min at 5000 rpm, and the supernatant collected was filtered through a Dismic (0.2 μm) syringe filter to remove any solids present. The concentration of the leached metals was determined through ICP-OES at room temperature.

Terephthalic acid probing technique

To detect $^{\bullet}OH$ generation by the decomposition of H_2O_2, three different treatment groups containing TA + H_2O_2, TA + MTV-1, and TA + MTV-1 + H_2O_2 were incubated in PBS (5.5) at 37 °C. The concentration of MTV-1 (50 μg mL^{-1}), TA (2 mM), and H_2O_2 (1 mM) was kept constant in each treatment group. Each treatment group was allowed to react for 2 h, and photoluminescence spectra under excitation of a wavelength of 315 nm and emission wavelength of 435 nm were recorded using a fluorescence spectrometer.[88]

Statistical analysis

All of the statistical analyses were performed using GraphPad Prism version 8.0. Data from the MTT assay was presented as mean ± standard deviation. The Kruskal–Wallis test, followed by Dunn's multiple comparison analysis, was performed to evaluate the statistically significant treatments from the control groups. A p-value equal to 0.05 or less was considered significant. The degree of significance from the control group is demonstrated as $^{****}p \leq 0.0001$, $^{***}p \leq 0.001$, $^{**}p \leq 0.01$, and $^{*}p \leq 0.05$. The IC_{50} values were calculated by fitting the cell

viability data into non-linear regression analysis and evaluating it through a dose–response curve.

Kinetic studies

Mathematical kinetic release models are applied to better understand the underlying mechanism of drug release from the nanocarriers.[89] Some of the widely used kinetic release models, such as zero-order, first-order, Higuchi, Korsmeyer–Peppas, and Hixson–Crowell, were applied in our study.[90,91] The formulae of these models are available in Table S4 (ESI†).

Results and discussion

Synthesis and characterization

Fabrication of MTV-MOFs consisted of a two-step approach. At first, a FeCo(μ_3-O) cluster was synthesized following a previously published route.[83] During the synthesis procedure, metal ions in the cluster are arranged triangularly and bridged with a central oxygen (μ_3-O) atom. The octahedrally coordinated metal ions are connected to the solvent molecules ($^-$OH, H_2O, and Cl^-) at their terminal positions. Acetate ions act as a bridge between each pair of metal ions allowing the cluster to adopt a specified tri-nuclear geometry.[92]

In the second step, pure phase FeCo-MIL-88B, FeCo-MIL-88D, and MTV-MOFs were synthesized by reacting the FeCo-(μ_3-O) cluster with individual and mixed linkers (BDC and BPDC) of varying stoichiometry. During the reaction, acetate ligands of the cluster were replaced by the carboxylates of reacting linkers in a dissociative manner, resulting in the formation of the desired MOF.[93] A total of five MOFs were synthesized based on the percentage mixing of the additional BPDC linker (0, 25, 50, 75 and 100%) and termed FeCo-MIL-88B, MTV-1, MTV-2, MTV-3, and FeCo-MIL-88D respectively. Various analytical techniques were utilized to characterize the synthesized nanocarriers. The samples' morphological appearance and metal composition were assessed through SEM, EDX, and ICP-OES. The SEM micrographs of the FeCo(μ_3-O) cluster show irregular morphology and a polycrystalline nature (Fig. S1a and b, ESI†), while the EDX, elemental maps (Fig. S1c and d, ESI†), and ICP-OES analysis of the metal composition revealed the homogenous distribution of Fe and Co in a 2 : 1 ratio (Table S1, ESI†). Similarly, SEM micrographs of the nanocarriers synthesized from the same cluster revealed hexagonal rod-shaped morphology similar to MIL-88B topology (Fig. 1).[94] However, a gradual increase in the size of crystals from FeCo-MIL-88B (190 ± 18 nm) to MTV-1 (364 ± 26 nm), MTV-2 (680 ± 32 nm), MTV-3 (1015 ± 58 nm) and FeCo-MIL-88D (1630 ± 62 nm) was observed by increasing the concentration of BPDC in the reaction mixture. The elemental composition of the MTV-1 MOFs in EDX and elemental mapping (Fig. 2a and b) also confirmed the homogenous distribution of both metals with a 2 : 1 ratio of Fe and Co.

The PXRD patterns of the simulated and synthesized FeCo-cluster are shown in Fig. S2a (ESI†). The synthesized PXRD pattern of the cluster matched well with the reported FeCo-cluster in the

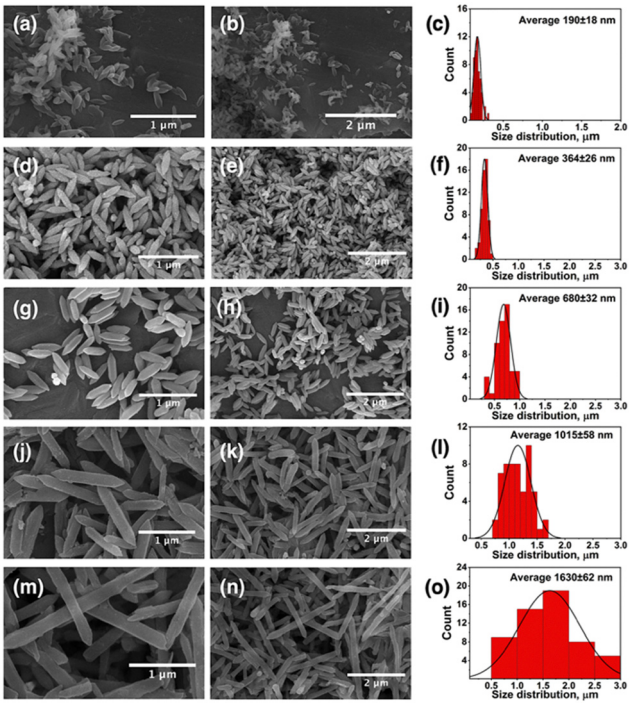

Fig. 1 SEM images of synthesized MOFs with their corresponding size distribution charts. (a)–(c) FeCo-MIL-88B, (d)–(f) MTV-1, (g)–(i) MTV-2, (j)–(l) MTV-3, and (m)–(o) FeCo-MIL-88D.

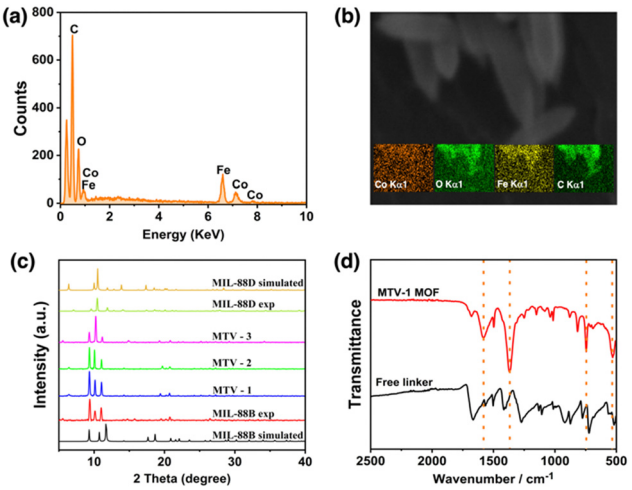

Fig. 2 The EDX (a) and elemental maps (b) of MTV-1. The PXRD pattern (c) of simulated and experimental MOFs, and FT-IR spectra (d) of MTV-1.

literature.[83] The PXRD pattern of the synthesized mono-linker MOFs exhibited high crystallinity evident from sharp peaks that matched well with the simulated MIL-88B and MIL-88D MOFs (Fig. 2c).[95,96] The synthesized MOFs revealed three characteristic peaks at 9.4 and 10.14° (2theta), corresponding to 002 and 100 planes. The third peak at 11.1° was attributed to the 101 plane of the open structure MIL-88B MOFs due to entrapped solvent molecules.[97]

The FT-IR spectra of the FeCo-cluster are shown in Fig. S2b (ESI†). In the FT-IR spectrum, the stretching at 726 cm^{-1} and

524 cm^{-1} represent the FeCo–O bonds in the cluster. The absence of a band at ~600 cm^{-1} corresponding to the monometallic Fe_3O cluster represents the broken D_{3h} symmetry to C_{2v} upon incorporating one Co atom in the structure, while the bands at 1577 cm^{-1} and 1409 cm^{-1} are related to the O–C–O asymmetric and symmetric stretching of the acetate ligands.[98,99] The reduction in the band gap from 320 to <240 cm^{-1} of the asymmetric and symmetric (1373 and 1606 cm^{-1}) vibrations of MTV-1 MOFs shows the coordination of the linker with metal clusters and the formation of MOFs.[100] The IR stretching around 1680 cm^{-1} in MTV-1 corresponds to the presence of coordinated DMF molecules in the structure (Fig. 2d). Based on the crystal size and cellular uptake kinetics,[101] MTV-1 MOFs (25% of BPDC) were only used for subsequent experiments in the study.

Fabrication of MTV-1@5-FU + CUR

The FT-IR spectra of 5-FU, CUR, MTV-1@5-FU + CUR, and activated MTV-1 are shown in Fig. 3a. In the FT-IR spectra of activated MTV-1, no peak around 1680 cm^{-1} related to the C═O group of DMF was observed indicating the activation of MTV-1 due to the evacuation of solvent molecules. In the FT-IR spectra of 5-FU, peaks found at 1731, 1240, and 800 cm^{-1} correspond to the C–N, C–O, and C–F stretching modes also found in MTV-1@5-FU + CUR.[102] The characteristic peaks related to CUR can also be seen in the FT-IR spectra of MTV-1@5-FU + CUR, indicating its incorporation.[103] According to the literature, CUR can coordinate with the central metal in a diketo form.[104] Since MTV-1 is composed of an oxo-centered trinuclear metal cluster (SBU) coordinated to removable H_2O molecules, some of these H_2O molecules are eliminated upon activation, leaving open metal sites/coordinatively unsaturated sites (CUSs).[105] The CUR molecules are capable of coordinating with these CUSs. As shown in the FT-IR spectra of free CUR (Fig. 3a), the vibrational stretching at 1496 and 1424 cm^{-1} indicates the existence of a free carbonyl group of enol and diketone form of CUR. In the FT-IR spectra of MTV-1@5-FU + CUR, the enolic form peak at 1424 cm^{-1} is absent, hinting at CUR's presence in diketo form. Some of the characteristic peaks of 5-FU and CUR present in MTV-1@5-FU + CUR are listed in Table S3 (ESI†).

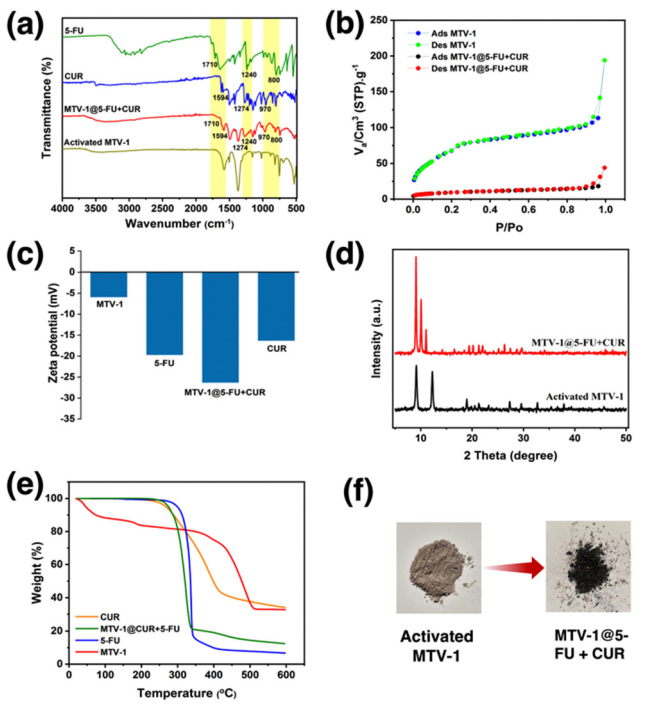

Fig. 3 FT-IR spectra (a), N_2 adsorption–desorption isotherm (b), zeta potential results (c), PXRD pattern (d), and TGA curves (e) of MTV-1 before and after drug loading. Digital photographs (f) of activated and dual-drug loaded MTV-1 MOFs.

The nitrogen sorption measurements exhibited differences in the BET surface due to the presence of distinct pores with FeCo-MIL-88B (110 $m^2\ g^{-1}$), MTV-1 (192 $m^2\ g^{-1}$) and FeCo-MIL-88D (382 $m^2\ g^{-1}$) (Fig. S3, ESI†). The increase in the surface area and pore heterogeneity can be observed after adding BPDC into the FeCo-MIL-88B MOFs. However, the surface area of the MTV-1 MOFs decreased from 192 to 29 $m^2\ g^{-1}$ after drug loading, highlighting the occupation of pores by drug molecules (Fig. 3b). Drug loading was also confirmed by electro-kinetic potential/zeta potential results (Fig. 3c). The reduced potential of MTV-1 after 5-FU and CUR loading suggests drug loading not just into the pores (confirmed by a reduction in BET surface area) but also on the surface of MTV-1.[106,107]

The PXRD pattern of activated MTV-1 and MTV-1@5-FU + CUR is shown in Fig. 3d. A shift from 10.8 to 12° (2theta) was observed in thermally activated samples due to cage shrinkage and elimination of trapped solvent molecules based on Bragg's law.[108] No significant change in the PXRD pattern of the activated MTV-1 and MTV-1@5-FU + CUR was observed. However, a shift in the peak of the 101 plane from 12° to 11.05° and the emergence of a peak at 10.4° of the 100 plane correspond to the open form of the structure due to reverse breathing and drug encapsulation.[109] Moreover, no extra peaks related to the crystalline form of drug molecules were seen in the PXRD pattern of MTV-1@5-FU + CUR, suggesting the presence of drug molecules in an amorphous form.

The TGA analysis of the samples is shown in Fig. 3e. The mass loss below the 300 °C temperature range was attributed to the evacuation of coordinated solvent/water molecules inside the structure. In contrast, the second mass loss from ~340 to 510 °C was due to the decomposition of the linkers and structural collapse.[110,111] The drug-loaded MTV-1@5-FU + CUR did not exhibit an initial mass loss pattern like MTV-1 and presented significant mass loss in the range of 270–340 °C related to the decomposition of drug molecules.[112,113] The TGA analysis further concludes the successful encapsulation of the drug molecules into the structure of MTV-1.

The amount of drugs loaded on the nanocarriers was checked through UV-vis spectroscopy based on the calibration curves of 5-FU (λ = 265 nm) and CUR (λ = 425 nm) in ethanol (Fig. S4 and S5, ESI†). The drug loading capacity (DLC) of the nanocarriers for 5-FU and CUR was found to be 15.9 and 9.3 wt%, while the drug loading efficiency (DLE) for 5-FU and CUR were 18.1 and 10.5 wt%, respectively.

Drug release

The pH-responsive drug release from MTV-1@5-FU + CUR was investigated in PBS buffer solutions under physiological (pH 7.4) and tumor microenvironment (pH 5.5) conditions (Fig. 4). It is well known that the cancer cell environment is acidic; thus, developing pH-responsive nanocarriers could be an effective strategy to enhance the selectivity and efficacy of therapeutics.[114,115] The dual-drug release profile of MTV-1@5-FU + CUR was monitored for 48 h based on the calibration curves of 5-FU and CUR in PBS +1%v/v Tween-80 (Fig. S6 and S7, ESI†). The release profile indicated a burst release of both drugs during the initial eight hours, releasing more than 21 and 37% of the loaded 5-FU and CUR at pH 5.5. The burst release of the drug during the first few hours can be attributed to the adsorbed drug molecules on the surface of the framework.[19] After the initial burst release, a gradual increase in the release was observed, leading to 50% of the loaded 5-FU being released after 32 h and CUR after 18 h at pH 5.5. While at pH 7.4, the percentage of 5-FU and CUR release stood at only 18% and 21% at the same time intervals.

The rapid drug release by the pH-responsive nanocarriers at lower pH is helpful in the accumulation of therapeutics in tumorigenic tissues, enhances efficacy, and reduces cytotoxicity to healthy cells.[116] The faster release of CUR from the carriers can be correlated with the protonation of CUR at lower pH.[117] The diketo oxygen atoms in the CUR act as proton sponges in an acidic environment with proton abundance resulting in a higher release of the drug from the carriers.[118] While 5-FU weakly binds to MOFs, which causes its quicker release in the simulated environment.[119] Another reason behind the rapid release of drug molecules under acidic pH (5.5) could be the MOF's linker protonation and structural decomposition.[120] As seen in the PXRD pattern of the MTV-1 samples soaked in PBS (5.5 and 7.4) for 48 h (Fig. 5a), the samples soaked in PBS (7.4) mostly retained their crystalline character. In comparison, the PXRD pattern of the nanocarriers immersed in PBS (5.5) resulted in the loss of prominent peaks related to the parent MOF. Additionally, extra peaks emerged around 17, 26, 31, and 45° (2theta), indicating the formation of Fe/Co phosphates.[121,122] The strong affinity of phosphate ions in PBS towards the accessible Fe/Co sites results in the release of carboxylate ligands and degradation of the structure.[123]

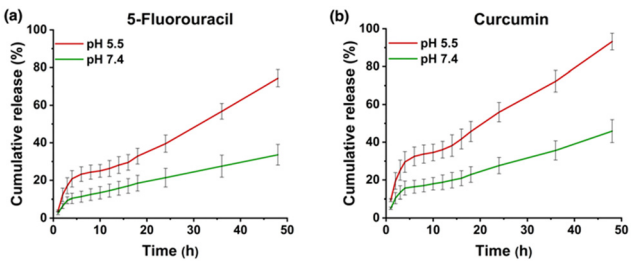

Fig. 4 Drug release profile of MTV-1@5-FU + CUR for 5-FU (a) and CUR (b) at different pH values (5.5 and 7.4).

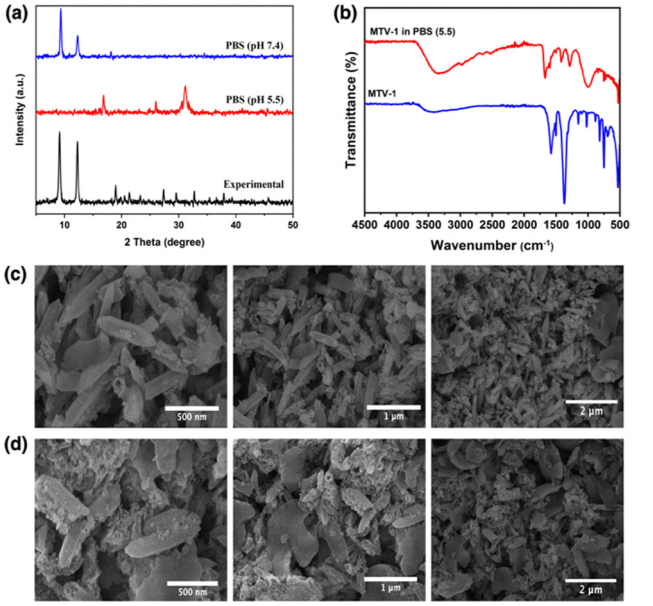

Fig. 5 PXRD pattern (a) of MTV-1 immersed in PBS (5.5 and 7.4), FT-IR spectra (b) of MTV-1 immersed in PBS (5.5), and SEM images of MTV-1 immersed in buffers of pH = 7.4 (c) and pH = 5.5 (d).

FT-IR further evaluated this to understand the variation in the atomic connectivity of the MTV-1 structure under PBS. As shown in Fig. 5b, significant changes in the vibrational stretching can be observed in the samples immersed in PBS (5.5). A visible decrease in the intensity of the metal-oxygen bonds around 725 cm^{-1} and 524 cm^{-1} is found in the spectra. The vibrational bands of the free linker around 1680 cm^{-1} (antisymmetric) and 1288 cm^{-1} (symmetric) can also be seen in the spectra of PBS-immersed samples.[124] Moreover, the broad band found around 1100 cm^{-1} to 920 cm^{-1} is related to the antisymmetric stretching of PO_4^{3-} groups.[125] Considering the strong attraction of phosphate groups towards polyvalent cations and the presence of the uncoordinated ligands' footprints, the data supports the analogy of drug release through structural decomposition.

SEM analysis also investigated the structural anomaly of the MTV-1 after immersion into different pHs. As shown in Fig. 5c, slight distortions in the morphology were found in the samples immersed in PBS (7.4), but the overall structure was retained. However, amorphous structures without appropriate morphology can be seen in samples immersed in PBS (5.5), which further supports the theory of rapid drug release due to structural decomposition (Fig. 5d).

Kinetic study

The drug release from a carrier depends on various factors, such as drug movement, carrier degradation, swelling, and interaction with guest molecules.[126] To better understand the drug release process, data from drug release studies were fitted into different mathematical kinetic release models and their formulas are presented in Table S4 (ESI†). These models are described below.

Zero-order

In zero-order release models, the release of encapsulated drug is time-dependent and follows a constant rate irrespective of the concentration of the drug.[127] The obtained data from the release studies are fitted by plotting cumulative drug release (%) against time. M_0 is the drug's initial concentration, M_t is the drug released over time t, and K_0 is the zero-order constant.

First-order

First-order release models describe that the relationship between time and concentration is always concentration-dependent. According to this model, the release amount of the drug always depends on the remaining drug concentration inside the carriers and tends to decrease over time.[128] M_0 is the initial concentration of the drug dissolved, M_t is the concentration of the drug released at time t, and K_1 is the first-order constant. The data is presented by plotting the log of cumulative (%) drug remaining against time.

Higuchi model

The Higuchi release model is based on Fick's law of diffusion and states that the drug release rate depends on diffusion. It is applied when the drug's initial concentration exceeds its solubility in the matrix.[129] In this model, M_t is the drug concentration released at time t, and KH is the release constant.

Korsmeyer–Peppas model

The Korsmeyer–Peppas model of drug release is applied when the release mechanism is unknown, the drug release is from a polymeric system, or two or more phenomena govern the drug release process.[130] The data are represented by plotting the log of cumulative drug release (%) against the log of time. Where M_t/M_∞ denotes fractional drug release at time t, k_{KP} is the Korsmeyer–Peppas release constant, and n is the release exponent.

Hixson–Crowell model

The volume and area of the carriers govern the Hixson–Crowell drug release model. It is applied when the drug release from the carriers is limited to the dissolution rate rather than diffusion.[131] The data is represented by plotting the cube root of the remaining drug (%) against time. M_t/M_∞ represents fractional drug release, and KHC is the Hixson–Crowell release constant.

The results obtained by fitting the different kinetic models (Fig. S8 and S9, ESI†) to the *in vitro* drug release profiles are presented in Table 1. It was found that drug release under normal pH favours zero order, first order, and the Hixson–Crowell model. In contrast, the correlation coefficient (R^2) was found to be higher in zero order for drug release in acidic pH. The R^2 value for acidic pH release was also higher in the Hixson–Crowell and Higuchi model. It can be concluded from the application of mathematical release models and their representative R^2 values that the main driving forces behind drug release at both pHs are diffusion and structural disintegration of MTV-1 MOFs.

Cytotoxicity assay and cellular uptake

The cytotoxicity effect of free 5-FU, CUR, MTV-1, and MTV-1@5-FU + CUR was carried out against HEK-293 and HepG2 cell lines using an MTT assay.[132] The cell viability results indicate dose-dependent growth inhibition of both cell lines. As shown in Fig. 6, with the increase in the concentration of treating agents, the viability of the cells decreased after 48 h. First, the cytotoxic profile of all treating agents was evaluated against HEK-293. The biocompatibility of any carrier against normal cells is always considered an essential step in developing efficient DDS.[133] The nanocarriers, which are target-specific, biodegradable, and present lower cytotoxic effects against normal cells, are mostly considered suitable for drug delivery applications.[13,101,134] Interestingly, MTV-1 did not show severe effects on the growth of HEK-293 cells and presented higher biocompatibility with an IC_{50} of 295.4 μg mL^{-1}. However, a lower percentage of viable cells was observed when HEK-293 cells were treated with the MTV-1@5-FU + CUR compared to free 5-FU and CUR.

The estimated IC_{50} values of the treating agents are shown in Table 2. In the case of HepG2 cells, a similar cell viability trend was observed for 5-FU, CUR, and MTV-1 with slight variation in the IC_{50} values. The MTV-1@5-FU + CUR exhibited enhanced cytotoxic effects against HepG2 cells compared to free 5-FU and CUR. Although the difference in the IC_{50} values of the applied MTV-1@5-FU + CUR and free drugs is not huge, it is essential to note the bioavailability of a free drug *vs.* an encapsulated one. Free drugs are readily available in the system, and the incubation time of a cytotoxicity assay might be enough to check their cytotoxicity. In contrast, an extended period of time is required to assess the cytotoxicity of a DDS as the drug release is time-constrained and not fully available to the system immediately.[135]

The statistically significant effects against the control groups for each treatment were represented as $^{****}p \leq 0.0001$, $^{***}p \leq 0.001$, $^{**}p \leq 0.01$, and $^{*}p \leq 0.05$. The IC_{50} values for MTV-1@5-FU + CUR against HepG2 cells (78.7 μg mL^{-1}) were found to be lower than HEK-293 (175.3 μg mL^{-1}). The cytotoxicity profile against the normal cells could be improved using surface

Table 1 Kinetic release model data based on the R^2 coefficient value of drug release and their fit into the models

Drug	pH	Parameters	Zero-order	First-order	Higuchi model	Korsmeyer–Peppas	Hixson–Crowell
5-FU	5.5	R^2	0.9688	0.8821	0.9447	0.9343	0.9399
	7.4		0.9644	0.9709	0.9432	0.9285	0.9707
CUR	5.5		0.9648	0.9419	0.9303	0.8973	0.9585
	7.4		0.9602	0.977	0.9792	0.9417	0.9723

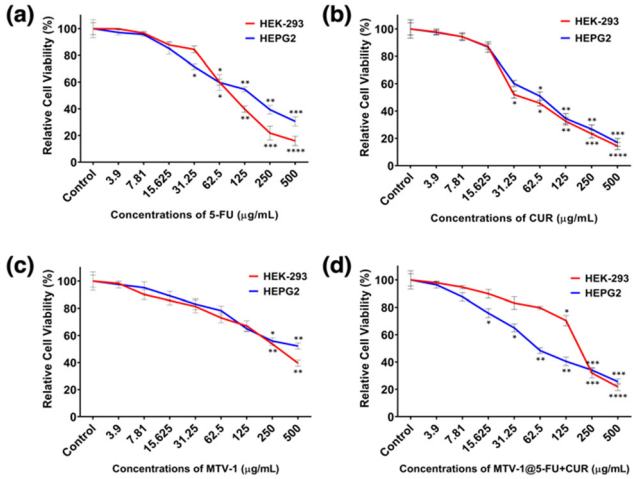

Fig. 6 Results related to the percentage cell viability of HEK-293 and HepG2 cell lines against different concentrations of 5-FU (a), CUR (b), MTV-1 (c), and MTV-1@5-FU + CUR (d) after 48 h. The degree of significance related to treatment groups against control groups in each cell line is shown as ****$p \leq 0.0001$, ***$p \leq 0.001$, **$p \leq 0.01$, and *$p \leq 0.05$.

Table 2 Estimated IC_{50} values of treatment groups against HEK-293 and HepG2 cells

	Treatment groups (μg mL^{-1})			
Cell lines	5-FU	CUR	MTV-1	MTV-1@5-FU + CUR
HEK-293	138.6	57.6	295.4	175.3
HepG2	93.9	68.5	423.9	78.7

chemistry to modify the nanocarriers with targeted biopolymer coatings reported in the literature.[136–139]

To evaluate the long-term anticancer efficacy of free 5-FU, CUR, MTV-1, and MTV-1@5-FU + CUR, colony-forming assay was performed in HepG2 cancer cell lines. The cells were treated with equal doses of 125 μg mL^{-1} of the samples and allowed to incubate for eight days. As shown in Fig. S10 (ESI†) a significant decrease in the number of colonies (>10-fold) in the cells treated with MTV-1@5-FU + CUR was observed compared with the control, free 5-FU, CUR, and MTV-1. These results were found in agreement with previous studies, which observed that nanocarriers encapsulated with chemotherapeutics showed a higher reduction in the colony formation ability of cancer cells compared with the free drug molecules.[140] Another reason behind the higher anti-colony formation activity of the MTV-1@5-FU + CUR is the synergistic effect of 5-FU and CUR against cancer cells. According to previous studies, dihydropyrimidine dehydrogenase (DPYD) expression is considered one of the major determinants in limiting 5-FU catabolism and efficacy.[141] While CUR is known to induce the P53 pathway which plays a key role in downregulating DPYD expression. Therefore, CUR synergistically enhances the cytotoxicity of 5-FU by indirect downregulation of DPYD expression.[142]

The potential of MTV-1 to be used as DDS was also evaluated through cellular uptake studies based on the intrinsic green

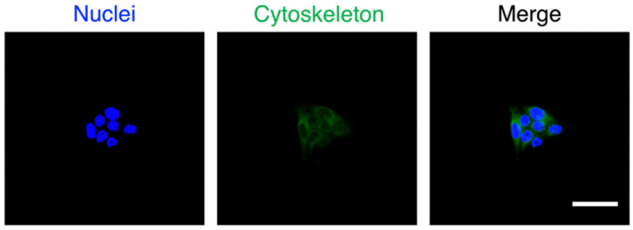

Fig. 7 The fluorescence images of cell nucleus (a) with blue fluorescence, stained by DAPI, MTV-1@5-FU + CUR (green fluorescence) (b), and overlay image (c) with scale bars = 20 μm.

fluorescence of CUR.[143] The fluorescence imaging results for the cellular uptake of MTV-1@5-Fu + CUR into HepG2 cells are presented in Fig. 7; the blue fluorescence represents the cell's nucleus stained by DAPI, and the detected green fluorescence is of CUR. The merged overlay image reveals the successful internalization of the MTV-1@5-FU + CUR by HepG2 cells, as green fluorescence of the CUR can be observed in the cytoplasmic area. Generally, the therapeutic ability of any anticancer drug depends on its effective delivery into the cytoplasm, accumulation, and retention for a sustained period.[144] Based on the results, the significant cytotoxicity of MTV-1@5-FU + CUR observed against HepG2 cell lines compared to free drugs could also be attributed to the successful internalization, accumulation and sustained release of both drugs encapsulated into the nanocarriers. Together, these results further suggest the potential of MTV-1@5-FU + CUR to be used as an effective DDS against HepG2 cancer cells.

Peroxidase like activity

Due to the frequent utilization of Fe and Co-based compounds as catalysts for redox reactions,[145,146] MTV-1 was investigated for their peroxidase-like characteristics using the 3,3′,5,5′-tetramethylbenzidine (TMB) oxidation method (Scheme 1).

TMB is a classic colourless chromogenic agent that tends to transform into a green-coloured oxidized form (ox-TMB) in the presence of H_2O_2 and a catalyst.[147] Mechanistic studies have revealed that H_2O_2 is first decomposed into highly reactive •OH radicals by the catalyst, and these •OH radicals in the second step oxidize the TMB present in the system.[148] As shown in Fig. 8a, no ox-TMB absorbance was observed at 652 nm when the system only contained H_2O_2 + TMB. In contrast, adding

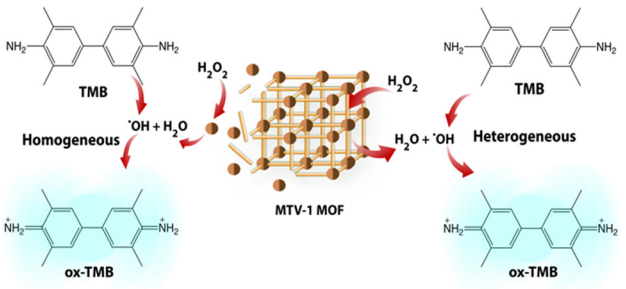

Scheme 1 Schematic representation of two-way channelled peroxidase-like activity of MVT-1 MOFs.

MOFs into the buffer system comprising H_2O_2 + TMB resulted in the change of colour and appearance of the absorption peak at 652 nm. This suggested that the peroxidase-like activity of our MOFs is similar to that of horseradish peroxidase (HRP). The desirable catalytic performance of the MTV-1 was also investigated by varying different factors, such as the system's catalyst concentration, temperature, and pH. In general, the catalytic reaction is accelerated by increasing the concentration of the catalyst, which was also observed in our case. The increase in catalyst concentration also increased the conversion of TMB into ox-TMB with increased colour intensity (Fig. 8a). Also, the optimal pH and temperature for the reaction were around 4 and 55 °C (Fig. 8b and c). The lower absorbance intensity of ox-TMB near physiological pH (7.4) verified the lesser •OH production under normal conditions, indicating the safety for normal tissues. On the contrary, the ox-TMB absorbance intensity enhanced with an increase in the system's acidity, which marked the higher catalytic activity of MTV-1 under acidic (tumor) conditions.

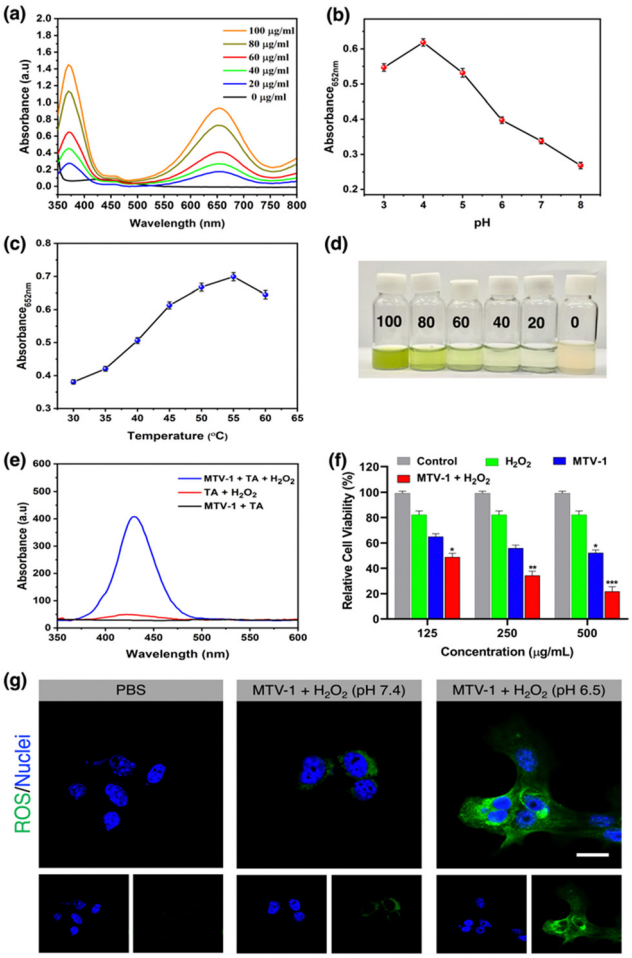

Fig. 8 Kinetic analyses of TMB oxidation by keeping the concentrations of TMB and H_2O_2 constant but varying the concentrations of MTV-1 MOFs (a), keeping all of the reactants constant but varying the pH (b), and temperature (c). Digital photographs of TMB colour change at different concentrations of MTV-1 (d), Fluorescence spectra of TA present in various reaction systems (e), cell viability of HepG2 cell line relative to the presence of MTV-1 with or without H_2O_2 (f) and confocal images of DCFH-DA and DAPI stained cells for intracellular •OH detection (g) scale bar = 20 μm.

Another reason behind the higher catalytic activity at lower pH is the leaching of free metal ions into the system. As confirmed by the ICP-OES studies, higher metal leaching activity was observed in the PBS (5.5) soaked MTV-1 samples as compared to PBS (7.4) (Fig. S11, ESI†). Various studies have observed that the reaction constant of free metal ions is many folds higher compared to the one coordinated to the structures.[149]

In this way, our MOFs not only produced •OH radicals at the surface (heterogeneous catalysis) but also through the leached Fe and Co metal ions in an acidic buffer (homogenous catalysis). These results further indicated the acid-sensitive intelligent Fenton-like catalytic performance of MTV-1. The higher release of Co ions compared to Fe ions is due to the weak Co^{II}–O coordination bonds prone to disintegration in the presence of competing water molecules in the medium.[150–152] Based on the hard and soft acid–base (HSAB) principle, under similar coordination environments, high-valent metals (Fe^{3+}, Cr^{3+}, Zr^{4+}, *etc.*) containing high charge density known as hard acids tend to make strong coordination bonds with oxygen donor ligands (carboxylate ligands) known as hard bases. Although carboxylate linkers have a lower pKa, high valent metal ions are linker-hungry for the maintenance of charge balance.[153] This leads to higher connectivity numbers of metal clusters with more linkers to further improve the resultant MOF stability.[154] However, low-valent metal ions, including Co^{2+}, Zn^{2+}, Ni^{2+}, *etc.*, are known as soft acids. Their coordination is usually more stable with N-containing linkers (soft bases) than oxygen donating linkers. In our case, the presence of one Co^{2+} per cluster resulted in loose coordination with BDC and BPDC, as both are O-donating linkers.[155] Therefore, in the presence of competing phosphate groups and water molecules, Co^{2+} ions were released faster as compared to high valent Fe^{3+} ions that have a strong coordination with the linker.[123,150]

To investigate the production of •OH radicals during the catalytic oxidation of TMB, a terephthalic acid (TA) probing technique was utilized.[156] The TA can quickly react with •OH and oxidize into a highly fluorescent 2-hydroxy terephthalic acid with characteristic fluorescence emission at 430 nm.[157] In our case, no fluorescence emissions of HTA were observed when H_2O_2 + TA or MTV-1 + TA were used. However, when MTV-1 was added to the H_2O_2 + TA solution, sharp fluorescence emission was monitored at 430 nm, suggesting the production of •OH during the oxidation process (Fig. 8e).

We further verified the Fenton-like catalytic performance of MTV-1 through a cell viability assay. As shown in Fig. 8f, less cell viability is observed in the MTV-1 treatment groups with the H_2O_2 compared to MTV-1 and H_2O_2 alone. This indicates the more potent anticancer activity of MTV-1 MOFs in the presence of H_2O_2 available in higher concentrations inside cancer cells. The intracellular ROS probe (DCFH-DA) further proved the •OH production in the HepG2 cellular environment. The MTV-1 gave a weak fluorescence signal at pH 7.4 compared to no signals from the control group. However, significant green emissions

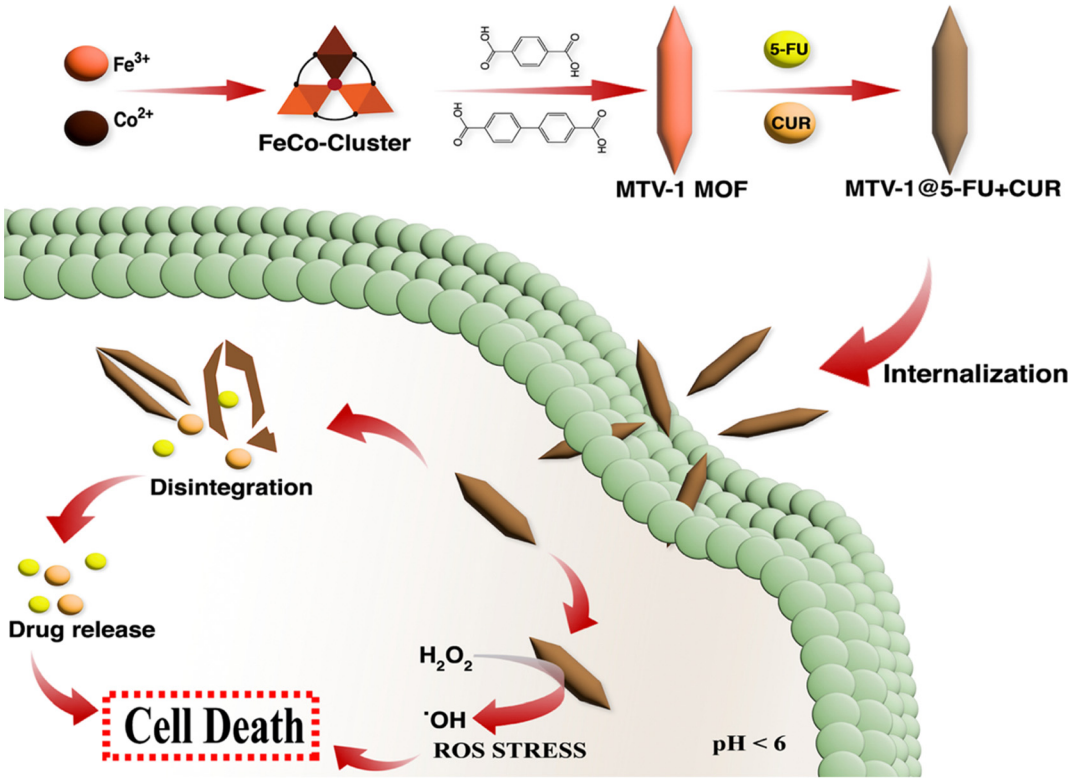

Scheme 2 Schematic illustration of MTV-1 MOF synthesis, the mechanism of pH-responsive drug delivery and ROS mediated multidimensional anticancer activity.

were recorded at pH 6.5, indicating the production of intracellular •OH in large amounts (Fig. 8g). The intracellular ROS studies signify the safety profile of MTV-1 against normal cells as very little signals of ROS production were detected at pH = 7.4 mimicking the physiological environment. Some of the recently reported MOFs for multifunctional co-delivery of drugs are presented in Table S5 (ESI†). Based on the results obtained, MTV-1, with pH-responsive dual-drug delivery and smart peroxidase-like activity (Scheme 2), could be used as a potential candidate for synergistic anticancer therapy.

Conclusion

We have established multivariate MOF carriers based on a mixed-ligand and metals approach. Using mixed ligands of varying lengths generated pores of varying sizes and facilitated the co-encapsulation of two anticancer drugs of different sizes. Drug loading and release experiments demonstrated that MTV-1 MOFs could carry a load of 15.9 and 9.3 wt% of 5-FU and CUR, respectively. These nanocarriers further exhibited pH-responsive drug release with higher concentrations of drugs released under cancer microenvironment conditions (pH 5.5) compared to conditions imitating a typical physiological environment (pH 7.4). The rapid release under a cancer cell environment is due to the collapse of the MTV-1's structure, confirmed by FT-IR, SEM, and XRD measurements. It shows the potential of MTV-1's to target cancer cells effectively. Moreover, the peroxidase-like catalytic activity of MTV-1 MOF ensured enhanced anticancer activity against HepG2 cells through a combination of chemotherapy and chemodynamic therapy. This work expands the dimensions of designing MOFs for co-encapsulation and delivery of multiple drugs through pore engineering. The results suggest the potential of multivariate MOFs to be used as potential candidates of DDS for multifunctional anticancer therapy.

Author contributions

M.U. Akbar: methodology, analysis and manuscript writing. A. Akbar: methodology. UAK. Saddozai: methodology and analysis. MIU. Khan: methodology. M. Zaheer: project supervision, funds management, manuscript editing and review. M. Badar: supervision, manuscript editing and review.

Conflicts of interest

The authors declare no conflict of interests.

Acknowledgements

This work was supported by the Faculty Initiative Fund (grant no. FIF-739) by the Lahore University of Management Sciences (LUMS). M.U.A acknowledges LUMS and Gomal University for providing technical support and a curriculum base for the

investigations in the project. The authors also extend their gratitude to The University of Lahore and Henan University for providing technical support in the project.

References

1 K. B. Tran, J. J. Lang, K. Compton, R. Xu, A. R. Acheson, H. J. Henrikson, J. M. Kocarnik, L. Penberthy, A. Aali and Q. Abbas, *Lancet*, 2022, **400**, 563–591.
2 D. Plana, A. C. Palmer and P. K. Sorger, *Cancer Discovery*, 2022, **12**, 606–624.
3 W. Liu, A. Dong, B. Wang and H. Zhang, *Adv. Sci.*, 2021, **8**, 2003033.
4 N. Vasan, J. Baselga and D. M. Hyman, *Nature*, 2019, **575**, 299–309.
5 H. Meng, W. X. Mai, H. Zhang, M. Xue, T. Xia, S. Lin, X. Wang, Y. Zhao, Z. Ji and J. I. Zink, *ACS Nano*, 2013, **7**, 994–1005.
6 S. Karimifard, N. Rezaei, E. Jamshidifar, S. Moradi Falah Langeroodi, M. Abdihaji, A. Mansouri, M. Hosseini, N. Ahmadkhani, Z. Rahmati and M. Heydari, *ACS Appl. Nano Mater.*, 2022, **5**, 8811–8825.
7 Q. Pan, J. Tian, H. Zhu, L. Hong, Z. Mao, J. M. Oliveira, R. L. Reis and X. Li, *ACS Biomater. Sci. Eng.*, 2020, **6**, 2175–2185.
8 F. Yaghoubi, N. S. H. Motlagh, S. M. Naghib, F. Haghiralsadat, H. Z. Jaliani and A. Moradi, *Sci. Rep.*, 2022, **12**(1), 1959.
9 Y. Wu, S. Lv, Y. Li, H. He, Y. Ji, M. Zheng, Y. Liu and L. Yin, *Biomater. Sci.*, 2020, **8**, 949–959.
10 L. Zhang, Z. Lin, Y. Chen, D. Gao, P. Wang, Y. Lin, Y. Wang, F. Wang, Y. Han and H. Yuan, *Eur. J. Pharm. Sci.*, 2022, **174**, 106199.
11 X. Liu, C. Wang, H. Ma, F. Yu, F. Hu and H. Yuan, *Adv. Healthcare Mater.*, 2019, **8**, 1801486.
12 X. Wan, J. J. Beaudoin, N. Vinod, Y. Min, N. Makita, H. Bludau, R. Jordan, A. Wang, M. Sokolsky and A. V. Kabanov, *Biomaterials*, 2019, **192**, 1–14.
13 F. Duda, M. Kieke, F. Waltz, M. E. Schweinefuß, M. Badar, P. P. Müller, K.-H. Esser, T. Lenarz, P. Behrens and N. K. Prenzler, *J. Mater. Sci.: Mater. Med.*, 2015, **26**, 1–8.
14 J. Yan, X. Xu, J. Zhou, C. Liu, L. Zhang, D. Wang, F. Yang and H. Zhang, *ACS Appl. Bio Mater.*, 2020, **3**, 1216–1225.
15 R. Cui, P. Zhao, Y. Yan, G. Bao, A. Damirin and Z. Liu, *Inorg. Chem.*, 2021, **60**, 1664–1671.
16 M. Cai, W. Liang, K. Wang, D. Yin, T. Fu, R. Zhu, C. Qu, X. Dong, J. Ni and X. Yin, *ACS Appl. Mater. Interfaces*, 2022, **14**, 36366–36378.
17 P. Horcajada, C. Serre, M. Vallet-Regí, M. Sebban, F. Taulelle and G. Férey, *Angew. Chem.*, 2006, **118**, 6120–6124.
18 S. Begum, Z. Hassan, S. Bräse, C. Wöll and M. Tsotsalas, *Acc. Chem. Res.*, 2019, **52**, 1598–1610.
19 S. Tarasi, A. Ramazani, A. Morsali, M.-L. Hu, S. Ghafghazi, R. Tarasi and Y. Ahmadi, *Inorg. Chem.*, 2022, **61**, 13125–13132.
20 X. Zhao, S. He, B. Li, B. Liu, Y. Shi, W. Cong, F. Gao, J. Li, F. Wang, K. Liu, C. Sheng, J. Su and H. Hu, *Nano Lett.*, 2023, **23**(3), 863–871.
21 A. Dutta, Y. Pan, J.-Q. Liu and A. Kumar, *Coord. Chem. Rev.*, 2021, **445**, 214074.
22 R. C. Huxford, J. Della Rocca and W. Lin, *Curr. Opin. Chem. Biol.*, 2010, **14**, 262–268.
23 R. K. Alavijeh and K. Akhbari, *Colloids Surf., B*, 2022, **212**, 112340.
24 Q. Jiang, M. Zhang, Q. Sun, D. Yin, Z. Xuan and Y. Yang, *Mol. Pharmaceutics*, 2021, **18**, 3026–3036.
25 S. Lawson, K. Newport, N. Pederniera, A. A. Rownaghi and F. Rezaei, *ACS Appl. Bio. Mater.*, 2021, **4**, 3423–3432.
26 C.-Y. Sun, C. Qin, X.-L. Wang and Z.-M. Su, *Expert Opin. Drug Delivery*, 2013, **10**, 89–101.
27 W. Cai, J. Wang, C. Chu, W. Chen, C. Wu and G. Liu, *Adv. Sci.*, 2019, **6**, 1801526.
28 Y. Zhang, F. Wang, E. Ju, Z. Liu, Z. Chen, J. Ren and X. Qu, *Adv. Funct. Mater.*, 2016, **26**, 6454–6461.
29 F. Oroojalian, S. Karimzadeh, S. Javanbakht, M. Hejazi, B. Baradaran, T. J. Webster, A. Mokhtarzadeh, R. S. Varma, P. Kesharwani and A. Sahebkar, *Mater. Today*, 2022, **57**, 192–224.
30 J. Dong, V. Wee and D. Zhao, *Nat. Mater.*, 2022, **21**, 1334–1340.
31 M. U. Akbar, M. Badar and M. Zaheer, *ACS Omega*, 2022, **7**, 32588–32598.
32 K. Li, J. Yang and J. Gu, *Chem. Mater.*, 2021, **33**, 2198–2205.
33 Y. Zhong, X. Li, J. Chen, X. Wang, L. Wei, L. Fang, A. Kumar, S. Zhuang and J. Liu, *Dalton Trans.*, 2020, **49**, 11045–11058.
34 J. Yang, S. Ma, R. Xu, Y. Wei, J. Zhang, T. Zuo, Z. Wang, H. Deng, N. Yang and Q. Shen, *J. Controlled Release*, 2021, **334**, 21–33.
35 B. Yang, L. Ding, H. Yao, Y. Chen and J. Shi, *Adv. Mater.*, 2020, **32**, 1907152.
36 G.-Y. Liou and P. Storz, *Free Radical Res.*, 2010, **44**, 479–496.
37 J. Wang and J. Yi, *Cancer Biol. Ther.*, 2008, **7**, 1875–1884.
38 H. Nakamura and K. Takada, *Cancer Sci.*, 2021, **112**, 3945–3952.
39 E. Novo and M. Parola, *Fibrog. Tissue Repair*, 2008, **1**, 1–58.
40 H. Ranji-Burachaloo, P. A. Gurr, D. E. Dunstan and G. G. Qiao, *ACS Nano*, 2018, **12**, 11819–11837.
41 A. D. Bokare and W. Choi, *J. Hazard. Mater.*, 2014, **275**, 121–135.
42 M. Cheng, C. Lai, Y. Liu, G. Zeng, D. Huang, C. Zhang, L. Qin, L. Hu, C. Zhou and W. Xiong, *Coord. Chem. Rev.*, 2018, **368**, 80–92.
43 X. Fu, Y. Zhang, G. Zhang, X. Li, S. Ni and J. Cui, *Appl. Mater. Today*, 2022, **26**, 101353.
44 S. Koo, O. K. Park, J. Kim, S. I. Han, T. Y. Yoo, N. Lee, Y. G. Kim, H. Kim, C. Lim and J.-S. Bae, *ACS Nano*, 2022, **16**, 2535–2545.
45 N. Xu, Q. Huang, L. Shi, J. Wang, X. Li, W. Guo, D. Yan, T. Ni, Z. Yang and Y. Yan, *Dalton Trans.*, 2023, **52**, 1687–1701.

46 Q. Shao, P. Wang and X. Huang, *Adv. Funct. Mater.*, 2019, **29**, 1806419.
47 S.-M. Hwang, S. J. Han, H.-G. Park, H. Lee, K. An, K.-W. Jun and S. K. Kim, *ACS Catal.*, 2021, **11**, 2267–2278.
48 Y. S. Lee, M. Yuan, R. Cai, K. Lim and S. D. Minteer, *ACS Catal.*, 2020, **10**, 6854–6861.
49 S. Chatterjee, K. Sengupta, S. Hematian, K. D. Karlin and A. Dey, *J. Am. Chem. Soc.*, 2015, **137**, 12897–12905.
50 W. N. Lanzilotta and L. C. Seefeldt, *Biochemistry*, 1997, **36**, 12976–12983.
51 M. Chen, Z. Long, R. Dong, L. Wang, J. Zhang, S. Li, X. Zhao, X. Hou, H. Shao and X. Jiang, *Small*, 2020, **16**, 1906240.
52 Q. Wu, M. S. Siddique, Y. Guo, M. Wu, Y. Yang and H. Yang, *Appl. Catal., B*, 2021, **286**, 119950.
53 X. Zhao, N. Zhang, T. Yang, D. Liu, X. Jing, D. Wang, Z. Yang, Y. Xie and L. Meng, *ACS Appl. Mater. Interfaces*, 2021, **13**, 36106–36116.
54 J. D. Evans, C. J. Sumby and C. J. Doonan, *Chem. Soc. Rev.*, 2014, **43**, 5933–5951.
55 S. Wongsakulphasatch, F. Nouar, J. Rodriguez, L. Scott, C. Le Guillouzer, T. Devic, P. Horcajada, J.-M. Grenèche, P. Llewellyn and A. Vimont, *Chem. Commun.*, 2015, **51**, 10194–10197.
56 C. Cao, X. Wang, N. Yang, X. Song and X. Dong, *Chem. Sci.*, 2022, **13**, 863–889.
57 R. Singh, A. Prasad, B. Kumar, S. Kumari, R. K. Sahu and S. T. Hedau, *ChemistrySelect*, 2022, **7**, e202201288.
58 M. X. Wu and Y. W. Yang, *Adv. Mater.*, 2017, **29**, 1606134.
59 H. D. Lawson, S. P. Walton and C. Chan, *ACS Appl. Mater. Interfaces*, 2021, **13**, 7004–7020.
60 H. Furukawa, U. Müller and O. M. Yaghi, *Angew. Chem., Int. Ed.*, 2015, **54**, 3417–3430.
61 M. Chen, J. Zhang, J. Qi, R. Dong, H. Liu, D. Wu, H. Shao and X. Jiang, *ACS Nano*, 2022, **16**, 7732–7744.
62 A. Kirchon, L. Feng, H. F. Drake, E. A. Joseph and H.-C. Zhou, *Chem. Soc. Rev.*, 2018, **47**, 8611–8638.
63 S. J. Lee, C. Doussot, A. Baux, L. Liu, G. B. Jameson, C. Richardson, J. J. Pak, F. Trousselet, F.-X. Coudert and S. G. Telfer, *Chem. Mater.*, 2016, **28**, 368–375.
64 T. M. Osborn Popp, A. Z. Plantz, O. M. Yaghi and J. A. Reimer, *Chem. Phys. Chem.*, 2020, **21**, 32–35.
65 Y. Fu, Z. Kang, W. Cao, J. Yin, Y. Tu, J. Li, H. Guan, Y. Wang, Q. Wang and X. Kong, *Angew. Chem.*, 2021, **133**, 7798–7806.
66 L. Zhu, F. Hu, B. Sun, S. Gu, T. Gao and G. Zhou, *Adv. Sustainable Syst.*, 2023, **7**, 2200394.
67 Y.-B. Zhang, H. Furukawa, N. Ko, W. Nie, H. J. Park, S. Okajima, K. E. Cordova, H. Deng, J. Kim and O. M. Yaghi, *J. Am. Chem. Soc.*, 2015, **137**, 2641–2650.
68 Y.-N. Zeng, H.-Q. Zheng, J.-F. Gu, G.-J. Cao, W.-E. Zhuang, J.-D. Lin, R. Cao and Z.-J. Lin, *Inorg. Chem.*, 2019, **58**, 13360–13369.
69 C.-C. Cao, C.-X. Chen, Z.-W. Wei, Q.-F. Qiu, N.-X. Zhu, Y.-Y. Xiong, J.-J. Jiang, D. Wang and C.-Y. Su, *J. Am. Chem. Soc.*, 2019, **141**, 2589–2593.
70 M. Carlsson, M. Gustavsson, G.-Z. Hu, E. Murén and H. Ronne, *PLoS One*, 2013, **8**, e52094.
71 N. Leelakanok, S. Geary and A. Salem, *J. Pharm. Sci.*, 2018, **107**, 513–528.
72 D. B. Longley, D. P. Harkin and P. G. Johnston, *Nat. Rev. Cancer*, 2003, **3**, 330–338.
73 M. H. Jouybari, S. Hosseini, K. Mahboobnia, L. A. Boloursaz, M. Moradi and M. Irani, *Colloids Surf., B*, 2019, **179**, 495–504.
74 Q. Fu, J. Wang and H. Liu, *Drug Delivery*, 2020, **27**, 1535–1543.
75 S. Pakian, F. Radmanesh, H. Sadeghi-Abandansari and M.-R. Nabid, *ACS Appl. Polym. Mater.*, 2022, **4**, 8238–8252.
76 S. Dhanavel, E. Nivethaa, V. Narayanan and A. Stephen, *Mater. Sci. Eng., C*, 2017, **75**, 1399–1410.
77 P. RS, A. Mal, S. K. Valvi, R. Srivastava, A. De and R. Bandyopadhyaya, *ACS Appl. Bio. Mater.*, 2020, **3**, 4643–4654.
78 P. Ratrey, S. V. Dalvi and A. Mishra, *ACS Omega*, 2020, **5**, 19004–19013.
79 M. Takahashi, S. Uechi, K. Takara, Y. Asikin and K. Wada, *J. Agric. Food Chem.*, 2009, **57**, 9141–9146.
80 B. H. Choi, C. G. Kim, Y. Lim, S. Y. Shin and Y. H. Lee, *Cancer Lett.*, 2008, **259**, 111–118.
81 G. A. Borges, S. T. Elias, B. Amorim, C. L. de Lima, R. D. Coletta, R. M. Castilho, C. H. Squarize and E. N. S. Guerra, *Phytother. Res.*, 2020, **34**, 3311–3324.
82 C. Mohanty, M. Das and S. K. Sahoo, *Expert Opin. Drug Delivery*, 2012, **9**, 1347–1364.
83 K. R. Sanchez-Lievanos, M. Tariq, W. W. Brennessel and K. E. Knowles, *Dalton Trans.*, 2020, **49**, 16348–16358.
84 M. Parsaei and K. Akhbari, *Inorg. Chem.*, 2022, **61**, 14528–14543.
85 A. Gerbino, G. Schena, S. Milano, L. Milella, A. F. Barbosa, F. Armentano, G. Procino, M. Svelto and M. Carmosino, *PLoS One*, 2016, **11**, e0156021.
86 W. Ni, L. Zhang, H. Zhang, C. Zhang, K. Jiang and X. Cao, *Inorg. Chem.*, 2022, **61**, 3281–3287.
87 Z. Wang, A. Von Dem Bussche, P. K. Kabadi, A. B. Kane and R. H. Hurt, *ACS Nano*, 2013, **7**, 8715–8727.
88 H. Ranji-Burachaloo, F. Karimi, K. Xie, Q. Fu, P. A. Gurr, D. E. Dunstan and G. G. Qiao, *ACS Appl. Mater. Interfaces*, 2017, **9**, 33599–33608.
89 M. L. Bruschi, *Strategies to modify the drug release from pharmaceutical systems*, Woodhead Publishing, 2015.
90 J. Dredán, I. Antal and I. Rácz, *Int. J. Pharm.*, 1996, **145**, 61–64.
91 G.-H. Son, B.-J. Lee and C.-W. Cho, *J. Pharm. Invest.*, 2017, **47**, 287–296.
92 L. Peng, M. Asgari, P. Mieville, P. Schouwink, S. Bulut, D. T. Sun, Z. Zhou, P. Pattison, W. Van Beek and W. L. Queen, *ACS Appl. Mater. Interfaces*, 2017, **9**, 23957–23966.
93 Q. Liu, H. Cong and H. Deng, *J. Am. Chem. Soc.*, 2016, **138**, 13822–13825.
94 L. Yang, T. Zhao, I. Boldog, C. Janiak, X.-Y. Yang, Q. Li, Y.-J. Zhou, Y. Xia, D.-W. Lai and Y.-J. Liu, *Dalton Trans.*, 2019, **48**, 989–996.

95 G.-T. Vuong, M.-H. Pham and T.-O. Do, *Dalton Trans.*, 2013, **42**, 550–557.
96 C. Serre, C. Mellot-Draznieks, S. Surblé, N. Audebrand, Y. Filinchuk and G. Férey, *Science*, 2007, **315**, 1828–1831.
97 P. Horcajada, C. Serre, G. Maurin, N. A. Ramsahye, F. Balas, M. Vallet-Regi, M. Sebban, F. Taulelle and G. Férey, *J. Am. Chem. Soc.*, 2008, **130**, 6774–6780.
98 M.-H. Pham, G.-T. Vuong, A.-T. Vu and T.-O. Do, *Langmuir*, 2011, **27**, 15261–15267.
99 T.-z Zhang, Y. Lu, Y.-g Li, Z. Zhang, W.-l Chen, H. Fu and E.-b Wang, *Inorg. Chim. Acta*, 2012, **384**, 219–224.
100 B. Iqbal, A. Laybourn and M. Zaheer, *Ceram. Int.*, 2021, **47**, 12433–12441.
101 N. Singh, S. Qutub and N. M. Khashab, *J. Mater. Chem. B*, 2021, **9**, 5925–5934.
102 A. R. Chowdhuri, D. Laha, S. Pal, P. Karmakar and S. K. Sahu, *Dalton Trans.*, 2016, **45**, 18120–18132.
103 A. Tiwari, A. Singh, N. Garg and J. K. Randhawa, *Sci. Rep.*, 2017, **7**, 1–12.
104 P. George, R. K. Das and P. Chowdhury, *Microporous Mesoporous Mater.*, 2019, **281**, 161–171.
105 J. N. Hall and P. Bollini, *React. Chem. Eng.*, 2019, **4**, 207–222.
106 S. Bhattacharjee, *J. Controlled Release*, 2016, **235**, 337–351.
107 B. Lei, M. Wang, Z. Jiang, W. Qi, R. Su and Z. He, *ACS Appl. Mater. Interfaces*, 2018, **10**, 16698–16706.
108 W. L. Bragg, *Scientia*, 1929, 23.
109 P. Horcajada, F. Salles, S. Wuttke, T. Devic, D. Heurtaux, G. Maurin, A. Vimont, M. Daturi, O. David and E. Magnier, *J. Am. Chem. Soc.*, 2011, **133**, 17839–17847.
110 R. I. Walton, A. S. Munn, N. Guillou and F. Millange, *Chem. – Eur. J.*, 2011, **17**, 7069–7079.
111 A. Schaate, P. Roy, A. Godt, J. Lippke, F. Waltz, M. Wiebcke and P. Behrens, *Chem. – Eur. J.*, 2011, **17**, 6643–6651.
112 J. Gandara-Loe, B. E. Souza, A. Missyul, G. Giraldo, J.-C. Tan and J. Silvestre-Albero, *ACS Appl. Mater. Interfaces*, 2020, **12**, 30189–30197.
113 S. Rojas, I. Colinet, D. Cunha, T. Hidalgo, F. Salles, C. Serre, N. Guillou and P. Horcajada, *ACS Omega*, 2018, **3**, 2994–3003.
114 X. Zhang, Y. Dong, X. Zeng, X. Liang, X. Li, W. Tao, H. Chen, Y. Jiang, L. Mei and S.-S. Feng, *Biomaterials*, 2014, **35**, 1932–1943.
115 Y. Yang, W. Zhu, L. Cheng, R. Cai, X. Yi, J. He, X. Pan, L. Yang, K. Yang and Z. Liu, *Biomaterials*, 2020, **246**, 119971.
116 I. A. Lázaro and R. S. Forgan, *Coord. Chem. Rev.*, 2019, **380**, 230–259.
117 H. Kalita, B. P. Kumar, S. Konar, S. Tantubay, M. K. Mahto, M. Mandal and A. Pathak, *Mater. Sci. Eng., C*, 2016, **60**, 84–91.
118 K. Akulov, R. Simkovitch, Y. Erez, R. Gepshtein, T. Schwartz and D. Huppert, *J. Phys. Chem. A*, 2014, **118**, 2470–2479.
119 X. G. Wang, L. Xu, M. J. Li and X. Z. Zhang, *Angew. Chem., Int. Ed.*, 2020, **59**, 18078–18086.
120 C. Adhikari, A. Mishra, D. Nayak and A. Chakraborty, *J. Drug Delivery Sci. Technol.*, 2018, **47**, 1–11.
121 C.-Z. Yuan, Y.-F. Jiang, Z. Wang, X. Xie, Z.-K. Yang, A. B. Yousaf and A.-W. Xu, *J. Mater. Chem. A*, 2016, **4**, 8155–8160.
122 A. M. Beale and G. Sankar, *J. Mater. Chem.*, 2002, **12**, 3064–3072.
123 X. Li, L. Lachmanski, S. Safi, S. Sene, C. Serre, J.-M. Grenèche, J. Zhang and R. Gref, *Sci. Rep.*, 2017, **7**, 13142.
124 Y.-S. Lin and K.-S. Lin, *Microporous Mesoporous Mater.*, 2021, **328**, 111456.
125 M. d J. Velásquez-Hernández, R. Ricco, F. Carraro, F. T. Limpoco, M. Linares-Moreau, E. Leitner, H. Wiltsche, J. Rattenberger, H. Schröttner and P. Frühwirt, *CrystEngComm*, 2019, **21**, 4538–4544.
126 X. Cai, M. Jin, L. Yao, B. He, S. Ahmed, W. Safdar, I. Ahmad, D.-B. Cheng, Z. Lei and T. Sun, *J. Mater. Chem. B*, 2022, 716–733.
127 M.-L. Laracuente, H. Y. Marina and K. J. McHugh, *J. Controlled Release*, 2020, **327**, 834–856.
128 P. Mazurek, M. A. Brook and A. L. Skov, *Langmuir*, 2018, **34**, 11559–11566.
129 F. R. Wibowo, O. A. Saputra, W. W. Lestari, M. Koketsu, R. R. Mukti and R. Martien, *ACS Omega*, 2020, **5**, 4261–4269.
130 A. Saravanan, M. Maruthapandi, P. Das, S. Ganguly, S. Margel, J. H. Luong and A. Gedanken, *ACS Appl. Bio Mater.*, 2020, **3**, 8023–8031.
131 C.-Y. Loo, R. Rohanizadeh, P. M. Young, D. Traini, R. Cavaliere, C. B. Whitchurch and W.-H. Lee, *J. Agric. Food Chem.*, 2016, **64**, 2513–2522.
132 Y.-L. Luo, Y.-S. Shiao and Y.-F. Huang, *ACS Nano*, 2011, **5**, 7796–7804.
133 C. Y. Ang, S. Y. Tan and Y. Zhao, *Org. Biomol. Chem.*, 2014, **12**, 4776–4806.
134 M. U. Akbar, S. Khattak, M. I. Khan, U. A. K. Saddozai, N. Ali, A. F. AlAsmari, M. Zaheer and M. Badar, *Front. Pharmacol.*, 2023, **14**, DOI: **10.3389/fphar.2023.1265440**.
135 P. F. Gu, H. Xu, B. W. Sui, J. X. Gou, L. K. Meng, F. Sun, X. J. Wang, N. Qi, Y. Zhang and H. B. He, *Int. J. Nanomed.*, 2012, 109–122.
136 M. Parsaei and K. Akhbari, *Inorg. Chem.*, 2022, **61**, 19354–19368.
137 S. Karimi and H. Namazi, *Int. J. Pharm.*, 2023, **634**, 122675.
138 J. Wu, S. Jiang, W. Xie, Y. Xue, M. Qiao, X. Yang, X. Zhang, Q. Wan, J. Wang and J. Chen, *J. Mater. Chem. B*, 2022, **10**, 8535–8548.
139 S. Mallakpour, F. Sirous and C. M. Hussain, *New J. Chem.*, 2021, **45**, 8409–8426.
140 B. Mansoori, A. Mohammadi, F. Abedi-Gaballu, S. Abbaspour, M. Ghasabi, R. Yekta, S. Shirjang, G. Dehghan, M. R. Hamblin and B. Baradaran, *J. Cell. Physiol.*, 2020, **235**, 6817–6830.
141 P. Gokare, N. K. Finnberg, P. H. Abbosh, J. Dai, M. E. Murphy and W. S. El-Deiry, *Sci. Rep.*, 2017, **7**, 9711.
142 W. Ni, Z. Li, Z. Liu, Y. Ji, L. Wu, S. Sun, X. Jian and X. Gao, *J. Pharm. Sci.*, 2019, **108**, 1284–1295.

143 A. Sahu, N. Kasoju and U. Bora, *Biomacromolecules*, 2008, **9**, 2905–2912.
144 M. M. Yallapu, M. Jaggi and S. C. Chauhan, *Colloids Surf., B*, 2010, **79**, 113–125.
145 T. Yang, D. Yu, D. Wang, T. Yang, Z. Li, M. Wu, M. Petru and J. Crittenden, *Appl. Catal., B*, 2021, **286**, 119859.
146 X. Liang, D. Wang, Z. Zhao, T. Li, Y. Gao and C. Hu, *Adv. Funct. Mater.*, 2022, **32**, 2203001.
147 W. Shi, Q. Wang, Y. Long, Z. Cheng, S. Chen, H. Zheng and Y. Huang, *Chem. Commun.*, 2011, **47**, 6695–6697.
148 H. Jiang, Z. Chen, H. Cao and Y. Huang, *Analyst*, 2012, **137**, 5560–5564.
149 M. Hermanek, R. Zboril, I. Medrik, J. Pechousek and C. Gregor, *J. Am. Chem. Soc.*, 2007, **129**, 10929–10936.
150 N. C. Burtch, H. Jasuja and K. S. Walton, *Chem. Rev.*, 2014, **114**, 10575–10612.
151 J. A. Greathouse and M. D. Allendorf, *J. Am. Chem. Soc.*, 2006, **128**, 10678–10679.
152 N. C. Burtch, I. M. Walton, J. T. Hungerford, C. R. Morelock, Y. Jiao, J. Heinen, Y.-S. Chen, A. A. Yakovenko, W. Xu and D. Dubbeldam, *Nat. Chem.*, 2020, **12**, 186–192.
153 M. Ding, X. Cai and H.-L. Jiang, *Chem. Sci.*, 2019, **10**, 10209–10230.
154 G. Férey, C. Mellot-Draznieks, C. Serre, F. Millange, J. Dutour, S. Surblé and I. Margiolaki, *Science*, 2005, **309**, 2040–2042.
155 X. C. Huang, Y. Y. Lin, J. P. Zhang and X. M. Chen, *Angew. Chem., Int. Ed.*, 2006, **45**, 1557–1559.
156 S. K. Maji, A. K. Dutta, D. N. Srivastava, P. Paul, A. Mondal and B. Adhikary, *J. Mol. Catal. A: Chem.*, 2012, **358**, 1–9.
157 K.-I. Ishibashi, A. Fujishima, T. Watanabe and K. Hashimoto, *J. Photochem. Photobiol., A*, 2000, **134**, 139–142.